

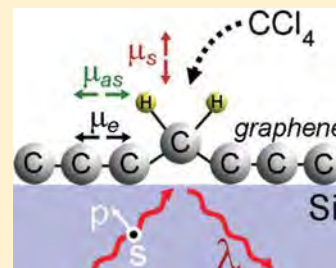
# Effects of Molecular Adsorption on the Electronic Structure of Single-Layer Graphene

V. M. Bermudez\* and J. T. Robinson

Electronics Science and Technology Division, Naval Research Laboratory, Washington, DC 20375-5347, United States

**S** Supporting Information

**ABSTRACT:** The interaction of small molecules ( $\text{CCl}_4$ ,  $\text{CS}_2$ ,  $\text{H}_2\text{O}$ , and acetone) with single-layer graphene (SLG) has been studied under steady-state conditions using infrared multiple-internal-reflection spectroscopy. Adsorption results in a broad and intense absorption band, spanning the  $\sim 200$  to  $500$  meV range, which is attributed to electronic excitation. This effect, which has not previously been reported for SLG, has been further investigated using dispersion-corrected density functional theory to model the adsorption of  $\text{H}_2\text{O}$  on SLG supported on an  $\text{SiO}_2$  substrate. However, the ideal and defect-free model does not reproduce the observed adsorption-induced electronic transition. This and other observations suggest that the effect is extrinsic, possibly the result of an adsorption-induced change in the in-plane strain, with important differences arising between species that form liquid-like layers under steady-state conditions and those that do not. Furthermore, the C–H stretching modes of  $\text{CH}_2$  groups, incorporated in the SLG as defects, undergo nonadiabatic coupling to the electronic transition. This leads to pronounced antiresonance effects in the line shapes, which are analyzed quantitatively. These results are useful in understanding environmental effects on graphene electronic structure and in demonstrating the use of the vibrational spectroscopy of H-containing defects in characterizing SLG structure.



## 1. INTRODUCTION

Changes in the electronic properties of single-wall carbon nanotubes (SWCNTs) and graphene, when brought into contact with molecular vapors, have long been recognized as a basis for chemical sensing<sup>1–3</sup> and for doping.<sup>4,5</sup> However, the mechanisms whereby these changes occur are in many cases not completely understood. In many interpretations, the substrate is described in terms appropriate to the Drude model for a free-electron gas. In this context, an electron donor or acceptor (e.g.,  $\text{NH}_3$  or  $\text{NO}_2$ , respectively) changes the density of free carriers and thereby the conductivity. For molecules with a significant dipole moment, a decrease in conductivity has been shown<sup>6</sup> to result from scattering of free carriers by the dipolar electric field. Such phenomena are well documented<sup>7</sup> in the case of adsorption on metals. Other processes, such as adsorbate-induced changes in the barrier height at the SWCNT/metal contact, have also been implicated.<sup>8</sup>

In the present work, it will be shown that weak electron acceptors ( $\text{CCl}_4$ ,  $\text{CS}_2$ ,  $\text{H}_2\text{O}$ ) and donors (acetone), especially in condensed liquid-like layers, can have a pronounced effect on the electronic structure of single-layer graphene (SLG). This will be detected, using infrared (IR) spectroscopy under steady-state conditions, through observation of changes in the broad-band absorption due to electronic excitation and of the coupling of local vibrational modes with this continuum. The line shape of the narrow vibrational resonance is sensitive to damping via nonadiabatic coupling to the electronic continuum, the nature of which can change when SLG interacts with an adsorbate. The electronic effects reported here constitute a potential new transduction mechanism for chemical sensing as well as a

framework for understanding environmental effects on the electronic properties of SLG.

Graphene layers were deposited on both sides of a lightly oxidized Si parallelepiped, configured for IR multiple-internal-reflection spectroscopy (MIRS), and characterized using X-ray photoemission spectroscopy (XPS) and Raman spectroscopy. The MIRS technique permits detection of surface species with high sensitivity under steady-state conditions, which is necessary due to the weak bonding interaction between SLG and the species of interest. For this study, the samples were not annealed, unless otherwise stated, so that the graphene would as much as possible resemble a “free-standing” layer. Annealing graphene in contact with  $\text{SiO}_2$  has been shown<sup>9</sup> to have pronounced effects on the chemical, physical, and electronic properties due to increased contact with the substrate.

## 2. EXPERIMENTAL DETAILS

**2.1. IR Spectroscopy.** The MIRS data were obtained using a Thermo Scientific 8700 Fourier-transform IR (FTIR) system with a liquid- $\text{N}_2$ -cooled “narrow-band”  $\text{Hg}_x\text{Cd}_{1-x}\text{Te}$  (MCT-A) detector at a resolution of  $4\text{ cm}^{-1}$ . 1000 scans were averaged in about 8 min, and 2-fold zero-filling and triangle apodization were applied to the interferogram before transformation. Polarization, when used, was provided by a wire-grid/KRS-5 device. The substrate was a  $25 \times 15 \times 1\text{ mm}^3$  float-zone (FZ) Si parallelepiped with a graphene film on both faces and an internal-reflection angle of  $\theta = 60^\circ$ . The use of FZ Si avoids the strong

**Received:** May 6, 2011

**Revised:** June 28, 2011

**Published:** August 03, 2011

Report Documentation Page				Form Approved OMB No. 0704-0188	
Public reporting burden for the collection of information is estimated to average 1 hour per response, including the time for reviewing instructions, searching existing data sources, gathering and maintaining the data needed, and completing and reviewing the collection of information. Send comments regarding this burden estimate or any other aspect of this collection of information, including suggestions for reducing this burden, to Washington Headquarters Services, Directorate for Information Operations and Reports, 1215 Jefferson Davis Highway, Suite 1204, Arlington VA 22202-4302. Respondents should be aware that notwithstanding any other provision of law, no person shall be subject to a penalty for failing to comply with a collection of information if it does not display a currently valid OMB control number.					
1. REPORT DATE <b>JUN 2011</b>		2. REPORT TYPE		3. DATES COVERED <b>00-00-2011 to 00-00-2011</b>	
4. TITLE AND SUBTITLE <b>Effects of Molecular Adsorption on the Electronic Structure of Single-Layer Graphene</b>				5a. CONTRACT NUMBER	
				5b. GRANT NUMBER	
				5c. PROGRAM ELEMENT NUMBER	
6. AUTHOR(S)				5d. PROJECT NUMBER	
				5e. TASK NUMBER	
				5f. WORK UNIT NUMBER	
7. PERFORMING ORGANIZATION NAME(S) AND ADDRESS(ES) <b>Naval Research Laboratory, Electronics Science and Technology Division, Washington, DC, 20375</b>				8. PERFORMING ORGANIZATION REPORT NUMBER	
9. SPONSORING/MONITORING AGENCY NAME(S) AND ADDRESS(ES)				10. SPONSOR/MONITOR'S ACRONYM(S)	
				11. SPONSOR/MONITOR'S REPORT NUMBER(S)	
12. DISTRIBUTION/AVAILABILITY STATEMENT <b>Approved for public release; distribution unlimited</b>					
13. SUPPLEMENTARY NOTES					
14. ABSTRACT <b>The interaction of small molecules (CCl<sub>4</sub>, CS<sub>2</sub>, H<sub>2</sub>O, and acetone) with singlelayer graphene (SLG) has been studied under steady-state conditions using infrared multipleinternal- reflection spectroscopy. Adsorption results in a broad and intense absorption band spanning the &amp;#8764;200 to 500 meV range, which is attributed to electronic excitation. This effect which has not previously been reported for SLG, has been further investigated using dispersioncorrected density functional theory to model the adsorption of H<sub>2</sub>O on SLG supported on an SiO<sub>2</sub> substrate. However, the ideal and defect-free model does not reproduce the observed adsorption-induced electronic transition. This and other observations suggest that the effect is extrinsic, possibly the result of an adsorption-induced change in the in-plane strain, with important differences arising between species that form liquid-like layers under steady-state conditions and those that do not. Furthermore, the C H stretching modes of CH<sub>2</sub> groups, incorporated in the SLG as defects undergo nonadiabatic coupling to the electronic transition. This leads to pronounced antiresonance effects in the line shapes, which are analyzed quantitatively. These results are useful in understanding environmental effects on graphene electronic structure and in demonstrating the use of the vibrational spectroscopy of H-containing defects in characterizing SLG structure.</b>					
15. SUBJECT TERMS					
16. SECURITY CLASSIFICATION OF:			17. LIMITATION OF ABSTRACT <b>Same as Report (SAR)</b>	18. NUMBER OF PAGES <b>11</b>	19a. NAME OF RESPONSIBLE PERSON
a. REPORT <b>unclassified</b>	b. ABSTRACT <b>unclassified</b>	c. THIS PAGE <b>unclassified</b>			

1106  $\text{cm}^{-1}$  O impurity band found in Czochralski Si. High-resistivity Si was used, as is typical in IR MIRS, to avoid strong free-carrier absorption.  $\theta$  was chosen to be much higher than the critical angle ( $\theta_c \approx 17^\circ$  for Si in the mid-IR) for two reasons. First, although a high  $\theta$  reduces somewhat the sensitivity to absorbing thin films,<sup>10</sup> it also minimizes the total optical path length through the Si, thus moving the transmission cutoff to lower energy.<sup>11</sup> Second, a high  $\theta$  reduces the possibility of anomalous internal-reflection phenomena<sup>10</sup> that can occur when  $\theta$  is close to  $\theta_c$ . The accessible range was  $\sim 1000\text{--}7500\text{ cm}^{-1}$ , limited on the low end by the Si transmission and on the high end by the detector response. Note that the spectrometer low-pass filter and the sampling interval had to be set appropriately to pass Fourier frequencies above the standard  $4000\text{ cm}^{-1}$  upper limit.

The substrate was mounted between two hollow blocks of Teflon and the whole assembly squeezed tightly together to form a vapor-tight seal around the edges of the Si. There were 11 internal reflections sampling graphene not in contact with Teflon. A stream of pure dry  $\text{N}_2$  was mixed with another stream of  $\text{N}_2$  saturated with the species of interest at the ambient-temperature vapor pressure ( $P_0$ ). The desired partial pressure ( $P/P_0$ ) was obtained by adjusting the flow rates of the two streams, which were then mixed and allowed to flow continuously over both faces of the sample while MIRS data were recorded. The total flow rate (both streams) was about 100 mL/min, with a total cell volume of 5.3 mL. Spectra are presented in the form of  $\delta R/R$ , the fractional change in reflectance per internal reflection caused by the introduction of the molecular species. The reference spectrum in all cases was obtained with pure  $\text{N}_2$  flowing through the cell. No smoothing or background correction was applied to any of the data.

Reagent-grade  $\text{CCl}_4$ ,  $\text{CS}_2$ , and acetone and locally prepared deionized  $\text{H}_2\text{O}$  were used without further purification and were contained in fritted gas-washing bottles, or "bubblers", through which dry  $\text{N}_2$  was flowed for preparation of the saturated  $\text{N}_2$  stream mentioned above. To check for impurities, the vapor stream exiting the Teflon cell could be directed through a 10 cm gas cell, with KBr windows, mounted in the FTIR sample compartment and the transmission spectrum compared to reference data. All liquids were degassed by purging with  $\text{N}_2$ . The liquid reservoirs were all at nominal room temperature ( $25^\circ\text{C}$ ) except for  $\text{CS}_2$ , which was maintained at  $5^\circ\text{C}$ . The vapor pressures at these temperatures are  $P_0 = 113, 158, 228$ , and  $23$  Torr, respectively, for  $\text{CCl}_4$ ,  $\text{CS}_2$ , acetone, and  $\text{H}_2\text{O}$  based on published parameters<sup>12</sup> ( $A, B$ , and  $C$ ) for the Antoine equation [ $\log_{10}(P_0) = A - B/(C + T)$ ].

**2.2. X-ray Photoemission and Raman Spectroscopies.** The XPS data were obtained using a Thermo Scientific K-Alpha system with a monochromated Al  $K\alpha$  source ( $h\nu = 1486.6\text{ eV}$ ) and a hemispherical electron energy analyzer at a resolution of about 0.6 eV. The area sampled was  $400\text{ }\mu\text{m}$  in diameter, and a flood gun was used for sample neutralization because the Si substrates used for MIRS are highly resistive. The BE was determined using a reference value<sup>13</sup> of 99.34 eV for the elemental Si  $2p_{3/2}$  peak. The BE correction required was small, typically  $\sim 0.1\text{ eV}$ . The C 1s least-squares fits were done using a Gaussian-broadened Doniach–Šunjić line shape for the graphene peak and pure Gaussians for other features, if any. These were added to a polynomial background function, and all parameters pertaining to the peak and the background were unconstrained in the fitting process.

Raman spectra were acquired using confocal Raman system with a single-mode 532 nm laser and a Princeton Instruments CCD array.

**2.3. Sample Preparation.** Graphene films were grown via low-pressure chemical vapor deposition (CVD) on Cu foils.<sup>14</sup> Twenty-five micrometer thick Cu foils (Alfa Aesar, 99.8%) were heated to  $1030^\circ\text{C}$  under flowing  $\text{H}_2$  at  $\sim 600\text{ mTorr}$  (with a system base pressure of  $\sim 5\text{ mTorr}$ ). At the growth temperature, the  $\text{H}_2$  pressure was decreased to  $<20\text{ mTorr}$ , and  $\text{CH}_4$  was introduced at pressures ranging from 40 to 300 mTorr and flow rates from 5 to 80 sccm for 15–45 min, after which the sample was quenched to room temperature. Methane pressures and

growth times were varied to adjust the density of bilayer islands from  $<\sim 4\%$  to approximately 40% coverage.

In another experiment, we attempted to introduce deuterium (D) into the films by flowing high-purity  $\text{D}_2/\text{CD}_4$  during growth under the same conditions described above for  $\text{H}_2/\text{CH}_4$ . However, as described in the main text, these films did not show evidence of D in the IR MIRS experiments. We speculate this may be due to (i) the presence of nondeuterated hydrocarbons during growth, (ii) D exchanging with H during the etching and transfer process (described below), or (iii) possibly atmospheric  $\text{H}_2\text{O}$  decomposing at defect sites in the film. The most likely location for C–H bonds in CVD graphene is at domain boundaries, vacancies, or free edges (such as those associated with isolated multilayer spots).

After growth, one side of the graphene-covered Cu foil was coated with poly(methyl methacrylate) (PMMA), and then the Cu/graphene/PMMA sample was floated in a Transene Cu etchant. Afterward, the PMMA/graphene film was transferred to a water bath. Films prepared in this manner were subsequently transferred onto both sides of a Si MIRS parallelepiped and then soaked in acetone to remove the PMMA. For two of the samples, post-transfer annealing was carried out in a 25 mm-diameter tube furnace with flowing Ar at atmospheric pressure at either  $T = 150^\circ\text{C}$  or  $T = 400^\circ\text{C}$  for 1 h.

### 3. RESULTS AND DISCUSSION

**3.1. Sample Characterization.** Figure 1a shows C 1s XPS data, which can be least-squares fitted with a single Gaussian-broadened Doniach–Šunjić (DS) function.<sup>15</sup> The DS theory describes the screening of a photoionized core hole in a free-electron

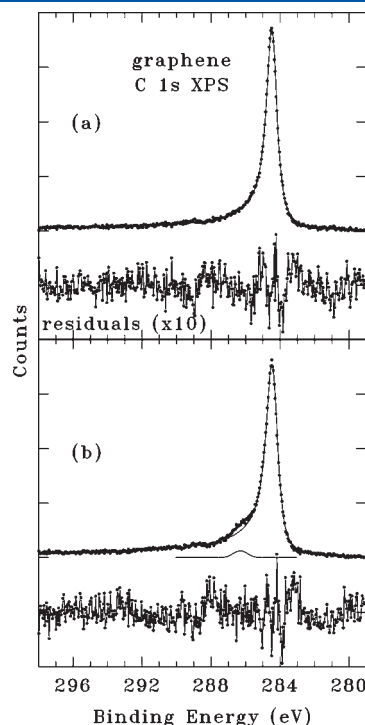


**Figure 1.** C 1s XPS data for a graphene sample (a) with no detectable O contamination (sample G1) and (b) with a small concentration of  $\text{sp}^3$  C–O bonds (sample G2). The points are the raw data after removal of the fitted polynomial background function. The lines are least-squares fits of a Gaussian-broadened DS function for the graphene peak and (in panel b) a pure Gaussian for the C–O satellite. The residuals (fit minus data, not statistically weighted) are shown multiplied by a factor of 10.

metal, which results in a distorted Lorentzian line shape with a tail extending to higher binding energy (BE). The DS function is only approximately accurate in the case of graphite,<sup>16</sup> which is a semimetal. Nevertheless, the fit shows only  $sp^2$ -hybridized C (BE = 284.5 eV) with little or no evidence of  $sp^3$ -hybridized C or of C–O bonds (as in C–O–C or C–OH groups). Such species would result in satellites<sup>17</sup> higher in BE by about 0.5 or 1.8 eV, respectively, than the  $sp^2$  C 1s peak. The DS asymmetry parameter ( $\alpha = 0.13$ ) agrees very well with the result<sup>16</sup> ( $\alpha = 0.125$ ) for bulk highly oriented pyrolytic graphite (HOPG). This sample, henceforth referred to as “G1” (for “graphene sample no. 1”), exhibited a C 1s intensity that was spatially uniform ( $\pm 10\%$ ) over most of both sides of the MIRS substrate, indicating a minimal density of holes (i.e., exposed  $SiO_2$ ).

Another sample (G2, Figure 1b) showed a weak satellite at 1.90 eV higher BE, with an integrated intensity equal to a few percent of that of the graphene peak, which indicates a small concentration of  $sp^3$  C–O bonds. There is also evidence in the residual spectrum of structure near 288 eV due to C=O bonds.<sup>17</sup> Some areas showed about the same C 1s intensity as did sample G1, but others showed a much smaller intensity, indicating holes in the graphene layer. A slightly larger DS asymmetry ( $\alpha = 0.17$ ) was needed to fit the graphene peak, which suggests the presence of a weak and unresolved  $sp^3$  component at slightly higher BE. Comparison of data for samples with different degrees of perfection will be useful in the following discussion. In all, five different SLG and three multilayer graphene samples were studied, and two of the SLG samples were subjected to annealing (to be discussed later), giving in effect a total of 10 samples. The XPS data in Figure 1 are representative of all of these samples. Analysis of the Si 2p XPS, described in section 1 of the Supporting Information, indicates an oxide layer underlying the graphene with a thickness in the range of 19–28 Å for all samples studied here. This layer is composed largely of  $SiO_2$  with little or no indication of suboxide features. The C 1s XPS data are discussed further in the Supporting Information, section 2. Two of the samples also showed a trace amount of Cu remaining from growth, but the Cu/C atom ratio was  $\leq 0.4\%$ . Additional sample characterization using Raman spectroscopy and optical microscopy is discussed in the Supporting Information, section 3.

**3.2. IR Spectroscopy Results – Overview and Electronic Excitation.** In this section, the general IR-spectroscopic results are described, and the adsorption-induced electronic excitation is examined. Figure 2 shows MIRS data (sample G1) for acetone,  $H_2O$ , and  $CCl_4$  (all at  $P/P_0 = 1.0$ , where  $P_0$  is the room-temperature vapor pressure) over a broad range from 1400 to 7000  $cm^{-1}$  (170–870 meV), which includes the strong  $\nu(C=O)$  carbonyl stretching mode of acetone (at 1715  $cm^{-1}$ ) and the  $\nu(OH)$  stretching and  $\delta(HOH)$  bending modes of  $H_2O$  (at  $\sim 3300$  and 1630  $cm^{-1}$ , respectively).  $CCl_4$  has no fundamentals in this range. Note that  $\delta R/R$  is defined such that downward-pointing peaks correspond to increased absorption due to the presence of the molecular layer. The  $\nu(C=O)$  peak appears at 1715  $cm^{-1}$ , which is characteristic of liquid acetone (vs 1738  $cm^{-1}$  for the vapor), indicating a condensed multilayer. The  $\nu(OH)$  region of  $H_2O$  shows evidence of overlapping bands at about 3380 and 3220  $cm^{-1}$ , the latter suggesting an ice-like ordering<sup>18,19</sup> at the graphene/ $H_2O$  interface. This aspect is beyond the scope of the present work, but the  $\nu(OH)$  structure is shown and discussed in more detail in the Supporting Information, section 4.

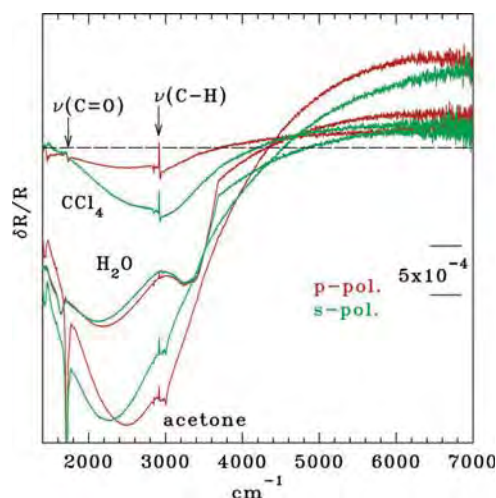


**Figure 2.** MIRS data for graphene (sample G1) exposed to acetone,  $H_2O$ , and  $CCl_4$  (all at  $P/P_0 = 1.0$ ). All spectra are shown on the same  $\delta R/R$  scale (normalized to the total number of internal reflections) and without any arbitrary vertical displacement. The dashed line shows the position of  $\delta R/R = 0$ . The increased noise at the high-energy end is due to decreasing detector sensitivity. The intense acetone  $\nu(C=O)$  peak at 1715  $cm^{-1}$  has been truncated for clarity of display. The structure at the low-energy end, near 1450  $cm^{-1}$ , results from a strong multiphonon absorption peak in the Si substrate that does not completely cancel in  $\delta R/R$ . The weak feature labeled “ $\nu(C=O)$ ” is due to an impurity discussed in the text. Note that an increase in absorption corresponds to downward-pointing peaks.

The weak feature at the extreme low-energy end of all spectra ( $\sim 1450$   $cm^{-1}$ ) is due to a strong Si multiphonon absorption that does not completely cancel in the ratio of single-beam spectra. A very weak structure, most noticeable in the p-polarized  $CCl_4$  spectrum, is seen near 1700  $cm^{-1}$  and is thought to arise from a perturbation of the  $\nu(C=O)$  mode<sup>20</sup> of carbonyl impurities by interaction with the liquid multilayer. Although such species are at or below the XPS detection limit ( $\sim 1\%$  of the graphene C 1s intensity, cf., Figure 1), they may be detectable in MIRS due to the large oscillator strength of this mode. However, there is no indication of the  $\nu(C=C)$  stretching mode, which, for defect-free SLG, is IR-forbidden<sup>21</sup> and not detected in transmission spectra.<sup>20</sup> This mode, which produces the Raman-active G-band found at 1588  $cm^{-1}$  in SLG, will be discussed later in connection with MIRS data for few-layer graphene (FLG).

The features of interest in the present work are the very intense and broad absorption bands spanning the  $\sim 1600$ – $4000$   $cm^{-1}$  (200–500 meV) range and the unusual line shapes seen in the  $\nu(C-H)$  stretching region ( $\sim 2850$ – $2950$   $cm^{-1}$ ). Purging with dry  $N_2$  at room temperature, following exposure to any of the species studied here, eventually removes these features. This indicates that they are not due to covalent bonding between the reagents and either graphene or the  $SiO_2$  underlayer. Rather, these effects are reversible at room temperature and are observable only under steady-state conditions. Numerical simulation of the MIRS experiment (Supporting Information, section 5) shows that they do not arise from thin-film optical effects,<sup>22</sup> and none of these effects were observed in “blank” experiments for which no graphene was deposited on the oxidized Si surface (Supporting Information, section 6). The blank sample was processed using the same procedure as for the graphene samples including the use, and subsequent removal, of PMMA as described above (section 2.3).



Further observations regarding the blank sample are given in the Supporting Information, sections 2 and 6.

Data obtained in the range of  $0.1 \leq P/P_0 \leq 1.0$  (not shown) indicate absorption intensities that increase with  $P/P_0$ . The absorption spectrum of ideal SLG does not exhibit any structure in this energy region.<sup>23</sup> It has been shown that movement of the Fermi level ( $E_F$ ) in bilayer graphene (BLG) or in FLG by electron transfer to or from an adsorbate<sup>24</sup> or by application of an electric field<sup>25–28</sup> can change the nature of the interband spectrum in the mid-IR. However, the interband transitions in BLG and FLG, which are modified by these perturbations, are not found in pristine SLG. Hence, the mechanisms discussed in refs 24–28 are not believed to be directly applicable to the present data. A subsequent section will discuss the effect of doping on the MIRS data; however, doping (i.e., a shift in  $E_F$ ) cannot by itself account for the appearance of a mid-IR absorption band in SLG. The Supporting Information, section 7, discusses similar data for sample G2, which has known imperfections as mentioned above. The spectra are quantitatively different, although broad-band absorptions and  $\nu(\text{C-H})$  line shape anomalies are again seen for all three adsorbates. For all samples, the intensity of the broad-band absorption consistently varies as  $\text{CCl}_4 < \text{H}_2\text{O} < \text{acetone}$ .

Numerical evaluation of the IR electric field throughout the MIRS sample (Supporting Information, section 8) shows that  $|E_{p,z}|^2$ , the intensity of the surface-normal component of the p-polarized field, is small within the graphene layer and that the in-plane field intensities,  $|E_{p,y}|^2$  and  $|E_{s,x}|^2$ , are relatively large and nearly equal. Hence, the dynamic dipole moment associated with the electronic excitation must lie in the SLG plane. Given the symmetry of ideal SLG, one then expects the s- and p-polarized spectra to be identical, which is not the case. This could be an indication of in-plane strain, which is found in theoretical work<sup>29,30</sup> to have a pronounced effect on the electronic structure of SLG. For certain directions, the effect of strain on the density of states (DOS) is particularly apparent near  $E_F$ , within the energy range studied here. Furthermore, the extent of the IR polarization dependence seen experimentally varies from sample to sample, which is consistent with an extrinsic effect such as strain. Hence, a change in strain due to contact with the liquid-like layer is tentatively suggested as a possible mechanism giving rise to the electronic absorption band. Buckling, or corrugation, is another well-known extrinsic effect in SLG supported on  $\text{SiO}_2$  (e.g., refs 9,31). However, this is found<sup>32</sup> not to affect the DOS near  $E_F$  except in extreme cases.

**3.3. Computational Model.** In this section, we consider whether the observed electronic absorption can be explained in terms of ideal SLG supported on  $\text{SiO}_2$ , using  $\text{H}_2\text{O}$  as the simplest adsorbate and one which is observed (Figure 2) to give a pronounced effect. There is also a body of prior theoretical work for  $\text{H}_2\text{O}/\text{SLG}$  with which to compare the present results. It has previously been proposed<sup>33,34</sup> that dangling-bond defects on the  $\text{SiO}_2$  surface are important in the response to adsorbates for SLG supported on  $\text{SiO}_2$ . However, any such highly reactive defects on air-exposed  $\text{SiO}_2$  would be passivated by dissociative adsorption of  $\text{H}_2\text{O}$  vapor to form OH groups and would not, therefore, be expected at a real graphene– $\text{SiO}_2$  interface.

Some density functional theory (DFT) treatments of  $\text{H}_2\text{O}$  on free-standing SLG have employed methods that do not completely account for dispersion (i.e., noncovalent or van der Waals interaction), which is expected to be a major factor in this system. The adsorption energies ( $\Delta E_{\text{ads}}$ ) found in these studies,<sup>33,35</sup>

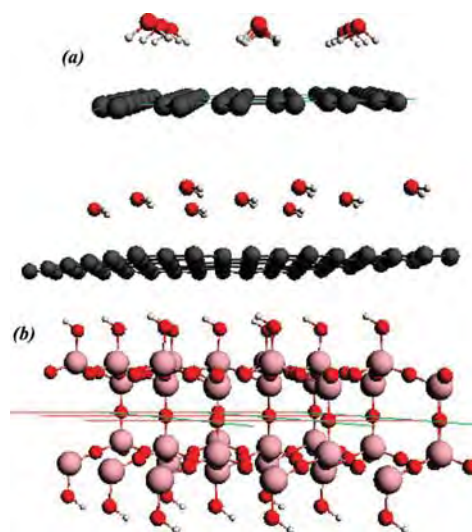


**Figure 3.** Computational results for the structure of  $\text{H}_2\text{O}$  on (a) free-standing SLG and on (b) SLG on  $\text{SiO}_2$ . In (b), a 7-layer, (111)-oriented slab is cut from the bulk  $\beta$ -cristobalite lattice and the under-coordinated Si atoms terminated with OH. A  $(2 \times 2)$  SLG supercell is placed on top, and one  $\text{H}_2\text{O}$  per supercell is added on top of the SLG. The atom colors are off-white (H), black (C), red (O), and beige (Si). See text and the Supporting Information, section 9, for further details.

using “pure” generalized gradient approximation functionals, have been  $\leq 40$  meV/ $\text{H}_2\text{O}$  with little or no effect on the graphene electronic structure near  $E_F$  for coverages up to a monolayer. On the other hand, studies using coupled-cluster methods<sup>36</sup> or symmetry-adapted perturbation theory,<sup>37</sup> which accurately treat dispersion,<sup>38</sup> find  $\Delta E_{\text{ads}}$  of 130–135 meV/ $\text{H}_2\text{O}$ . Other work,<sup>39</sup> using dispersion-corrected DFT, finds a smaller  $\Delta E_{\text{ads}}$  but one that is still larger than when noncovalent interaction is neglected. These studies all agree that in the lowest-energy configuration (Figure 3a)  $\text{H}_2\text{O}$  is oriented normal to the surface with the H atoms downward (i.e., closer than O to the graphene). However, the effects, if any, on the SLG electronic structure were not reported.

We have performed DFT calculations similar to those described in ref 33 but employing methods that include dispersion. Full details are given in the Supporting Information, section 9. The goal is to determine whether dispersion, which increases  $\Delta E_{\text{ads}}$ , also affects the SLG electronic structure near  $E_F$ . A coverage of 0.25  $\text{H}_2\text{O}$  per SLG unit cell was used, which (Supporting Information, section 9) is close to the coverage of “terminal”  $\text{H}_2\text{O}$  on the (0001) surface of hexagonal ice. Thus, the calculation simulates, in effect, SLG in contact with a hypothetical monolayer of ice. For free-standing SLG, a  $\Delta E_{\text{ads}}$  of 207 meV/ $\text{H}_2\text{O}$ , not corrected for basis set superposition error (BSSE), was found. The lack of a BSSE correction, which would reduce the magnitude of  $\Delta E_{\text{ads}}$ , makes it difficult to compare this result with previous reports.<sup>36,37,39</sup> However, without dispersion, no binding (i.e.,  $\Delta E_{\text{ads}} \approx 0$ ) was found, confirming the importance of including this effect. In this preliminary study, we have not determined the effect of higher  $\text{H}_2\text{O}$  coverages. Even with dispersion, no effect due to  $\text{H}_2\text{O}$  was seen in the DOS (not shown) within  $\sim 1.5$  eV of  $E_F$ . Also, no doping was observed, in the form of a shift of  $E_F$  into the valence or conduction band, because this appears<sup>33</sup> only for an  $\text{H}_2\text{O}$  multilayer with ice-like ordering.

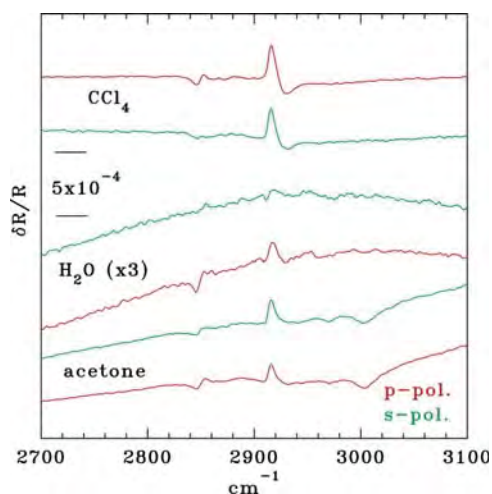


**Figure 4.** Similar to Figure 2 but showing the  $\nu(\text{C-H})$  region. The  $\delta R/R$  scale applies to the acetone and  $\text{CCl}_4$  data. The  $\text{H}_2\text{O}$  spectra have been multiplied by a factor of 3, and different spectra have been displaced vertically for clarity.

Following ref 33,  $\text{SiO}_2$  was included using a slab (Figure 3b) derived from the (111) surface of  $\beta$ -cristobalite with dangling Si bonds terminated in OH. The lattice constant of  $\beta$ -cristobalite is  $a_0 = 7.16 \text{ \AA}$ ; hence, that of the (111) surface unit cell ( $a_0/\sqrt{2}$ ) is only  $\sim 2.7\%$  larger than twice that of graphene. Thus, a  $(2 \times 2)$  SLG supercell is commensurate with a slightly compressed  $\beta$ -cristobalite (111) surface. Previous work<sup>33</sup> (omitting dispersion) for SLG interacting with defect-free  $\text{SiO}_2$  reported no significant effects in the vicinity of the SLG Fermi level, and the present results concur with this finding. The present work allows an estimate of the energy of adhesion between SLG and  $\text{SiO}_2$  as  $E_{\text{adh}} = E(\text{SiO}_2) + E(\text{SLG}) - E(\text{SiO}_2 + \text{SLG})$ , where  $E$  is the total energy after geometry relaxation. The result is  $E_{\text{adh}} = 320 \text{ meV}$  (not corrected for BSSE), which, upon normalization to the area of the  $(2 \times 2)$  SLG supercell, gives  $1.5 \text{ eV/nm}^2$ . This can be compared to a value of about  $0.50 \text{ eV/nm}^2$  ( $80 \text{ mJ/m}^2$ ) obtained<sup>40</sup> for vitreous  $\text{SiO}_2$  and graphite using molecular mechanics with a parametrized force field.

The next step is to add  $\text{H}_2\text{O}$  to the  $\text{SiO}_2$ -supported SLG. In the relaxed structure (Figure 3b),  $\text{H}_2\text{O}$  lies nearly flat, with  $\Delta E_{\text{ads}} = 257 \text{ meV/H}_2\text{O}$ . The difference of  $50 \text{ meV/H}_2\text{O}$  in  $\Delta E_{\text{ads}}$  from that for free-standing SLG given above should be essentially unaffected by BSSE. Thus, the underlying  $\text{SiO}_2$  slightly enhances the adsorption of  $\text{H}_2\text{O}$ ; however, there is again no effect on the DOS near  $E_F$ . It is concluded that pristine SLG is weakly hydrophilic but that the MIRS results cannot be explained simply in terms of an ideal  $\text{H}_2\text{O/SLG/SiO}_2$  structure and that some extrinsic effect, such as strain, is needed to account for the data.

**3.4. IR Spectroscopy Results – Vibrational Line Shapes and Fine Structure.** We now proceed to the anomalous  $\nu(\text{C-H})$  line shapes. Figure 4 shows the same data as in Figure 2 but focusing on the C–H stretching region. All three adsorbates gave similar features near  $2920$  and  $2850 \text{ cm}^{-1}$ , although they are relatively weak in the case of  $\text{H}_2\text{O}$ . A reason for the small effect of  $\text{H}_2\text{O}$  will be suggested in the following section. These features are reproducible for all 10 samples, and spectra obtained at  $2 \text{ cm}^{-1}$  (vs  $4 \text{ cm}^{-1}$ ) resolution showed a negligible reduction in line width, indicating that the data are not resolution limited. The higher-energy feature is essentially independent of polarization, whereas the lower-energy component is stronger in p-polarization.

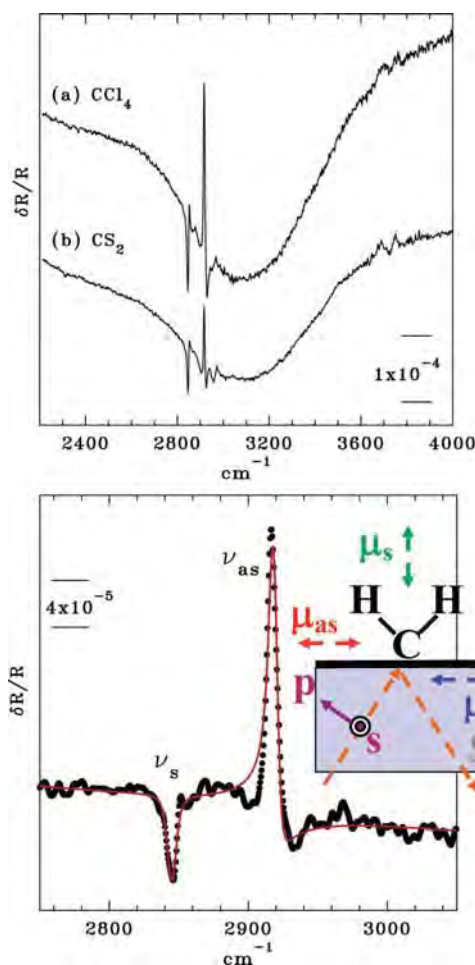


**Figure 5.** (Top) Data obtained under steady-state exposure to (a)  $\text{CCl}_4$  and (b)  $\text{CS}_2$  at  $P_0 = 99 \text{ Torr}$  ( $22^\circ\text{C}$ ) and  $158 \text{ Torr}$  ( $5^\circ\text{C}$ ), respectively, with an unpolarized IR beam. The data were obtained for sample G2, and the spectra have been displaced vertically for clarity. The weak structure near  $3700 \text{ cm}^{-1}$  is a baseline artifact. (Bottom) Least-squares fit of eq 1 to an s-polarized  $\text{CCl}_4$  spectrum. The points are the raw data, after subtraction of the fitted polynomial background, and the solid line is the fit. Note the different energy scales in the upper and lower panels. The fitting parameters are:  $\nu_0 = 2918 \text{ cm}^{-1}$ ,  $\nu_0 t = -3.49$ ,  $\Gamma_G = 4.6 \text{ cm}^{-1}$ ,  $\Gamma_L = 4.7 \text{ cm}^{-1}$ ; and  $\nu_0 = 2844 \text{ cm}^{-1}$ ,  $\nu_0 t = -0.01$ ,  $\Gamma_G = 5.3 \text{ cm}^{-1}$ ,  $\Gamma_L = 4.2 \text{ cm}^{-1}$ . The inset shows a configuration of the  $\text{CH}_2$  that is consistent with the different  $\nu_0 t$  results (see text). The dashed lines show the IR beam, and the s- and p-vectors define the polarizations.  $\mu_s$ ,  $\mu_{\text{as}}$ , and  $\mu_e$  depict the vibrational and electronic DDMs. The rotation of the  $\text{CH}_2$  about the surface normal is arbitrary; hence,  $\nu_s$  can be excited only by the surface-normal component in p-polarization, but  $\nu_{\text{as}}$  can be excited by s-polarization and by the in-plane component in p-polarization.

However, in the case of  $\text{H}_2\text{O}$ , the very weak  $\nu(\text{C-H})$  structure does show a polarization dependence, being almost undetectable in s-polarization. Additional structure is seen for acetone near  $3000 \text{ cm}^{-1}$  due to the molecular  $\nu(\text{C-H})$  modes. It should be noted that the graphene was not intentionally hydrogenated; hence, the  $\nu(\text{C-H})$  modes are due to defects and/or edge sites.

The following discussion will focus on the  $\text{CCl}_4$  results because  $\text{CCl}_4$  presents no interfering absorption bands in the region of interest and is “inert” in the sense of having no dipole moment and only a weak interaction with graphene-like materials.<sup>41</sup> Figure 5 compares data obtained during exposure to  $\text{CCl}_4$  and

to CS<sub>2</sub>, another small, nonpolar molecule with no C–H bonds. The results are clearly very similar. These data were obtained for sample G2 and are in good agreement with the CCl<sub>4</sub> data for sample G1 (Figure 2). As mentioned above (section 2.3), unsuccessful attempts were made to incorporate D using CD<sub>4</sub> and D<sub>2</sub> in place of CH<sub>4</sub> and H<sub>2</sub> in the growth. However, it was later determined that nondeuterated hydrocarbons were also present in the growth ambient and were possibly the source of the persistent CH<sub>x</sub> species. Hence, it cannot yet be determined at what point in the sample growth and preparation the C–H bonds are formed. Because the CH<sub>x</sub> groups involve sp<sup>3</sup> sites, a firm upper limit of ~0.1 is estimated for the CH<sub>x</sub>/total-C atomic ratio, based on the maximum possible sp<sup>3</sup>/sp<sup>2</sup> ratio in the C 1s XPS (Supporting Information, section 2).

The energies of the 2850 and 2920 cm<sup>-1</sup> peaks are consistent with, respectively, the symmetric (in-phase,  $\nu_s$ ) and asymmetric (out-of-phase,  $\nu_{as}$ ) C–H stretching modes<sup>42</sup> of an sp<sup>3</sup>-hybridized CH<sub>2</sub> group, which would be a defect in SLG. The line shape of the  $\nu_{as}$ (CH<sub>2</sub>) mode is unusual, being distorted and inverted or derivative-like in appearance. This effect is much less pronounced, and may even be absent, in the  $\nu_s$ (CH<sub>2</sub>) mode. The anomalous line shape results from the coupling of the vibrational mode to the electronic excitation continuum. The theory for this effect (termed “antiresonance”, “vibronic interference”, or “the Fano effect”) was developed in the context of adsorbate vibrational spectra by Langreth et al.<sup>43,44</sup> and reviewed from an experimental perspective by Chabal.<sup>45</sup> The dynamic dipole moment (DDM,  $\mu$ ) is the sum of a nuclear ( $\mu^n$ ) and an electronic ( $\mu^e$ ) component. In the case of coupling,  $\mu^n$  and  $\mu^e$  are out of phase resulting in a complex DDM given by  $\mu = \mu' + i\mu'' = \mu'(1 + i\omega\tau)$ , which leads to an asymmetric line shape.

Antiresonance in the IR spectra of adsorbates has been seen for H on W(100) and Mo(100) where the first overtone of the metal-H bending mode couples to a broad continuum of surface-state excitations.<sup>46</sup> It has also been seen for CO on Cu(100), where the frustrated rotation of the CO couples to the continuum of adsorbate-induced surface-state excitations.<sup>47</sup> Antiresonance has been observed<sup>24</sup> for the 1589 cm<sup>-1</sup> in-plane ( $E_{1u}$ )  $\nu$ (C=C) phonon in FLG, where the strength of the electron–phonon coupling was varied using adsorption of an electron donor (NH<sub>3</sub>) to shift  $E_F$ . The shift in  $E_F$  induces interband transitions that can then couple to the  $E_{1u}$  phonon. A similar effect has been observed<sup>25–27</sup> by applying an electric field to BLG to open a band gap, in which case the strength of the coupling varies as the gap is increased to coincide with the phonon energy. The present result is, however, fundamentally different from those of previous studies because it involves SLG interacting with molecules having relatively little (vs NH<sub>3</sub> or NO<sub>2</sub>) electron donor or acceptor character. Another form of coupling between electronic and vibrational excitations has been seen<sup>20</sup> in reduced graphene oxide (RGO). This is different from the effect studied here because in the case of RGO there is no phase difference between the vibrational and electronic excitations and, therefore, no antiresonance. In RGO, the electronic absorption results from the displacement of the O atoms in the  $\nu$ (C=O) mode and is therefore in phase with the atomic motion.

In all of the examples noted above, as well as in the present study, antiresonance involves an in-plane-polarized vibrational mode coupling to an in-plane-polarized electronic transition. Coupling is seen here (and in refs 20 and 24–27) only for vibrational modes involving species within the graphene layer

(e.g., C=C bonds or impurity C=O or C–H sites) and not for those involving adsorbates. Thus, the C atom involved in the vibrational mode must be a graphene site for strong coupling to occur. For example, Liu et al.<sup>24</sup> observe a three-peaked  $\nu$ (C–H) structure in the 2850–2950 cm<sup>-1</sup> range, which is characteristic of an aliphatic hydrocarbon<sup>42</sup> (possibly adsorbed from the ambient) and which does not exhibit antiresonance. Furthermore, none of the acetone molecular modes seen in the present work exhibit any line shape anomalies. Thus, the internal vibrational modes of the weakly bound molecular adsorbates studied to date do not themselves couple strongly to graphene electronic transitions. It is possible, however, that a strongly chemisorbed species would exhibit antiresonance as in the examples of H and CO on metals cited above.

Figure 5 shows a fit of representative s-polarized CCl<sub>4</sub> data with the antiresonance line shape function for an isolated oscillator derived by Crljen and Langreth,<sup>44</sup> which (with  $\omega = 2\pi\nu$ ) is given by<sup>45</sup>

$$\text{Im}[\alpha(\nu)] = \frac{\nu_0\mu'^2}{\pi} \left[ \frac{\nu\tau^2}{\Gamma_L} + \frac{\nu\Gamma_L(1 - \nu^2\tau^2) - 2\nu\tau(\nu^2 - \nu_0^2)}{(\nu^2 - \nu_0^2)^2 + \nu^2\Gamma_L^2} \right] \quad (1)$$

and which, for  $\tau = 0$ , reduces to the Lorentzian line shape. Here,  $\alpha(\nu)$  is the local polarizability,  $\Gamma_L$  is the Lorentzian line width, and all other terms have been defined previously. An s-polarized spectrum was used because the relative intensity of the lower-energy  $\nu_s$  peak is weaker than in p-polarization, which simplifies the fit. The fitting is made difficult by the presence of overlapping weak and poorly resolved structure due to overtones of the  $\delta$ (C–H) bending modes<sup>42</sup> and to the stretching modes of other C–H sites, which are not included in the fit. Evidence for the existence of other C–H sites will be given below.  $\alpha(\nu)$  was convoluted with a Gaussian (full-width at half-maximum, FWHM,  $=\Gamma_G$ ) to include inhomogeneous broadening and finite spectrometer resolution, both approximated as Gaussians. To this was added a cubic or quartic polynomial background function, and all terms were unconstrained in the fit.

The  $\Gamma_G$  values (given in the figure caption) are about the same for either peak, as are the two  $\Gamma_L$  values. Subtracting the FTIR resolution (4 cm<sup>-1</sup>) in quadrature from  $\Gamma_G$  gives an inhomogeneous broadening of about 2.3 (3.5) cm<sup>-1</sup> for the  $\nu_{as}$  ( $\nu_s$ ) mode. The main difference is in  $\nu_0\tau$ , a dimensionless asymmetry parameter that reflects the strength of the coupling between the electronic and vibrational excitations and that is large for the 2918 cm<sup>-1</sup>  $\nu_{as}$  mode and small for the 2844 cm<sup>-1</sup>  $\nu_s$ . Fits to other data sets give somewhat different results for  $\nu_0\tau$ , but the value for  $\nu_{as}$  ( $\nu_s$ ) is always in the range of –2.0 to –3.5 (0 to –0.5). For comparison,  $\nu_0\tau$  in the range of –1.6 to +0.54 has been found<sup>46,47</sup> for adsorbates on metals. The Supporting Information, section 10, shows how the line shape changes over a range of  $\nu_0\tau$  values and how these shapes replicate those seen in Figure 4.

The DDM of  $\nu_s$  is parallel to the 2-fold ( $C_2$ ) axis of the CH<sub>2</sub> group, whereas that of  $\nu_{as}$  is perpendicular to the  $C_2$  axis and lies in the CH<sub>2</sub> plane. Figure 5(inset) shows a configuration in which the CH<sub>2</sub> bridges two C atoms and lies above the SLG plane and which is consistent with the fitting results. It is not clear whether the CH<sub>2</sub> exists as a strained, cyclopropane-like structure or forms as a result of buckling of the graphene plane in response to the breaking of C=C bonds. Here, the  $\nu_s$  DDM is normal to the



surface and therefore unable to couple to  $\mu_e$ , whereas the  $\nu_{as}$  DDM can interact strongly. Deviations from this geometry in which the  $\nu_s$  DDM has a finite projection on the SLG plane will increase (decrease) the magnitude of  $\nu_o\tau$  for  $\nu_s$  ( $\nu_{as}$ ). In this model,  $\nu_s(\text{CH}_2)$  is completely p-polarized. However, the observed  $\nu_s/\nu_{as}$  relative intensity is about 1/3 (2/3) in s- (p-) polarization, not corrected for the relative magnitudes of the different components of the evanescent electric field (Supporting Information, section 8). The fact that  $\nu_s(\text{CH}_2)$  is not completely p-polarized (i.e.,  $\nu_s/\nu_{as}$  is nonzero in s-polarization) constitutes an apparent violation of the selection rule for this geometry. This could result from the buckling<sup>9,31</sup> (or corrugation) of SLG supported on  $\text{SiO}_2$ , which would tip the  $\text{C}_2$  axis away from the z-axis, as described in the Supporting Information, section 11.

A recent study,<sup>48</sup> using sum-frequency generation (SFG), reported the vibrational spectrum of individual H atoms chemisorbed as  $\text{sp}^3$  C–H groups on pristine SLG grown in situ in an ultrahigh vacuum on an Ir(111) surface. Because the s-polarized IR electric field is suppressed at the vacuum/metal surface,<sup>45</sup> only modes with a DDM normal to the surface were detected. These were superimposed on a broad continuum due to electronic excitation in the metal. This excitation (which is nonresonant with, and therefore does not couple to, the vibrational modes) is caused by the visible laser used in SFG. Antiresonance would still be possible, in principle, if the IR laser were to excite an electronic transition in the SLG at the frequency of a C–H stretching mode. However, no coupling was observed, which is consistent with the present results. In the experimental configuration used in ref 48, the SLG is in effect a metallic layer on a metallic substrate, and the DDM due to any IR-active electronic excitation within the SLG (or the Ir) would lie parallel to the surface<sup>45–47</sup> and, therefore, orthogonal to the DDM of the observed C–H modes. It is also noted that the observed SFG frequencies (2563 and 2716  $\text{cm}^{-1}$ , respectively, for ortho and para C–H pairs) are much lower than the frequencies of the  $\text{CH}_2$  defect sites seen here.

The effects on the  $\nu(\text{C–H})$  spectrum of annealing are now considered briefly. Temperature-programmed desorption (TPD) studies<sup>49</sup> of H on carbon nanosheets show several  $\text{H}_2$  peaks from  $\sim 450$  to 1100 K, indicating a variety of different adsorption sites and bonding configurations. Because similar TPD data for low coverages of H on SLG are, to our knowledge, unavailable, the nanosheet results are used as a guide. Annealing at 423 K (i.e., just below the desorption onset<sup>49</sup>) in flowing Ar had no significant effect on the  $\nu(\text{C–H})$  spectrum (not shown). However, annealing at 673 K, which decomposes some nanosheet  $\text{sp}^3$  C–H sites, caused major changes as shown in Figure 6. In addition to the overall loss in intensity, indicating removal of C–H bonds, there is a slight shift of both modes to higher energy.

A major effect is seen in  $\nu_s(\text{CH}_2)$ , which now exhibits a strongly antiresonant (inverted) line shape resembling that of  $\nu_{as}(\text{CH}_2)$ . This, and the fact that  $\nu_s(\text{CH}_2)$  is independent of IR polarization after annealing (not shown), indicates that the remaining  $\text{CH}_2$  has the DDMs of both  $\nu(\text{C–H})$  modes lying in the SLG plane. This accounts for the lack of polarization dependence, because both modes can now be excited by both  $E_{p,y}$  and  $E_{s,x}$  (Supporting Information, section 8), and for the strong coupling of both modes to the electronic DDM. Figure 6(inset) shows the implicit structure schematically. An in-plane  $\text{sp}^3$  (tetrahedral)  $\text{CH}_2$  group is difficult to envision in SLG; hence, we are led to consider a structure like a terminal  $\text{C}=\text{CH}_2$  group, which might occur at a vacancy or domain boundary in the SLG or at the periphery of the small BLG patches that are known to

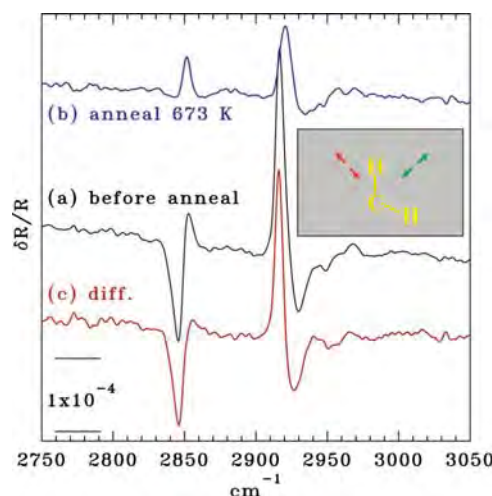


**Figure 6.** The effect of annealing on the  $\nu(\text{C–H})$  spectrum. The data show  $\delta R/R$  (p-polarized) for  $\text{CCl}_4$  exposure at  $P/P_0 = 1.0$  for an as-formed sample (a) and for the same sample after a 673 K vacuum anneal (b). Trace (c) shows the difference (a – b), and spectra have displaced vertically for clarity. The inset shows schematically a  $\text{CH}_2$  configuration, viewed along the z-axis (i.e., the surface normal) that is consistent with spectrum (b). The  $\text{CH}_2$  lies mainly in the SLG plane (gray), as do the  $\nu_s$  (green) and  $\nu_{as}$  (red) DDMs. The  $\text{CH}_2$  rotation about the surface normal is arbitrary.

exist in these samples. However, in organic molecules,  $\nu(\text{C–H})$  for such species typically falls above  $\sim 3050$   $\text{cm}^{-1}$ . Hence, the structure after annealing cannot yet be assigned conclusively. There may also be an effect resulting from the increased contact<sup>9</sup> between graphene and  $\text{SiO}_2$  after annealing.

Again using the nanosheet  $\text{H}_2$  TPD results<sup>49</sup> as a guide, we assume that the species remaining after the 673 K anneal are also present, in the same chemical state and in the same concentration, before annealing. We then subtract the spectrum after annealing from that recorded before annealing to obtain the difference, shown in Figure 6c, which represents the spectrum of the  $\text{sp}^3$   $\text{CH}_2$  species removed by annealing. This is qualitatively similar to the fitted line shape shown in Figure 5, which exhibits a “normal”  $\nu_s$  and a strongly antiresonant  $\nu_{as}$  mode. In this context, small sample-to-sample variations in the exact C–H line shapes, which are evident in comparing Figures 4–6, can be understood in terms of varying relative contributions from different C–H bonding configurations.

As a final comment, we have considered (Supporting Information, section 12) the possibility of an electrostatic contribution to the observed antiresonance line shapes arising from a coupling between the  $\nu(\text{C–H})$  dynamic dipole and the dipole induced in a polarizable adsorbate such as  $\text{CCl}_4$ . The conclusion is that such an effect cannot account for the observed line shapes.

**3.5. Additional Experiments.** In an effort to understand better the effects reported above, we now discuss three further experiments involving (i) analyte desorption, (ii) multilayer ( $>1$  layer) graphene films, and (iii) the effect of doping.

Figure 7 shows MIRS data versus elapsed time during  $\text{N}_2$  purging after exposure to acetone vapor at  $P/P_0 = 1.0$ . Acetone was selected because it gives an intense electronic absorption band and because the  $\nu(\text{C=O})$  mode is sensitive to the molecular environment.<sup>50</sup> The acetone modes, the  $\nu(\text{C–H})$  features, and a large part of the electronic absorption band all vanish within  $\Delta t = 1$  min, which is the maximum attainable time resolution in the present experiment. The remaining features are a weakened



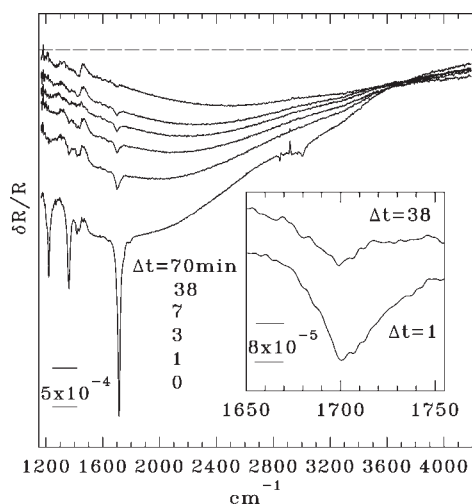


**Figure 7.**  $\delta R/R$  (unpolarized) versus elapsed time ( $\Delta t$ ) during purging with pure  $N_2$  after exposure to acetone vapor at  $P/P_0 = 1.0$ . Only 100 scans in  $\sim 50$  s were averaged, and  $\Delta t$  is the elapsed time at the end of the data collection. The  $\Delta t = 0$  spectrum was recorded prior to shutting off the acetone flow. The feature appearing near  $1450\text{ cm}^{-1}$ , with nearly constant intensity in all spectra, is a miscanceled Si multiphonon absorption.

electronic absorption band, which gradually shifts to higher energy with continued purging, and a weak  $\nu(C=O)$  peak that slowly loses intensity. The  $\nu(C=O)$  feature is broad and red-shifted to  $1700\text{ cm}^{-1}$  from the vapor-phase value of  $1738\text{ cm}^{-1}$ , indicating<sup>50</sup> a moderately strong interaction with a range of polar surface sites, which may include PMMA residue as well as regions of bare  $SiO_2$  (Supporting Information, section 6). Even for  $\Delta t$  as short as 1 min, there is no sign of remnant liquid acetone in the form of a sharp  $\nu(C=O)$  feature at  $1715\text{ cm}^{-1}$ . Corresponding data obtained as  $P/P_0$  is increased from zero (not shown) are consistent with these results. For  $P/P_0$  below  $\sim 0.3$ , the weak red-shifted  $\nu(C=O)$  and the weak electronic absorption band are seen. With increasing  $P/P_0$ , the electronic band gains intensity and shifts to lower energy, while the acetone modes become evident. The  $\nu(C-H)$  anti-resonance features can be seen, with low intensity, at  $P/P_0$  as low as 0.05 and saturate in intensity at  $P/P_0 \approx 0.6$ .

It is inferred from these data that the electronic absorption results from an essentially local effect. At high  $P/P_0$ , the whole SLG layer is wetted, including the nonpolar  $C-H$  sites, which do not bond strongly to acetone. In this case, the electronic perturbation extends over the entire SLG layer, and the anti-resonance is detected clearly. At lower  $P/P_0$ , acetone is bound mainly at polar sites, and the electronic perturbation is confined to the vicinity of these sites, which probably consist of a low concentration of O-containing defects. The  $C-H$  sites are, at this point, uncovered and not strongly affected by acetone.

The slow desorption evident in Figure 7 might also indicate that, at high  $P/P_0$ , some acetone enters the space between SLG and  $SiO_2$  from which it is slow to escape during purging. This gap has been measured<sup>51</sup> to be  $\sim 8.2\text{ \AA}$  for as-prepared SLG/ $SiO_2$  and is assumed to be filled with ambient species such as adsorbed  $H_2O$ . However, data given in the Supporting Information, section 13, show that acetone does not enter this space, although  $D_2O$  vapor easily exchanges with the  $H_2O$  underlayer. In any case, the local nature of the effect of acetone on SLG is consistent with the proposal that it is related to adsorption-induced strain.

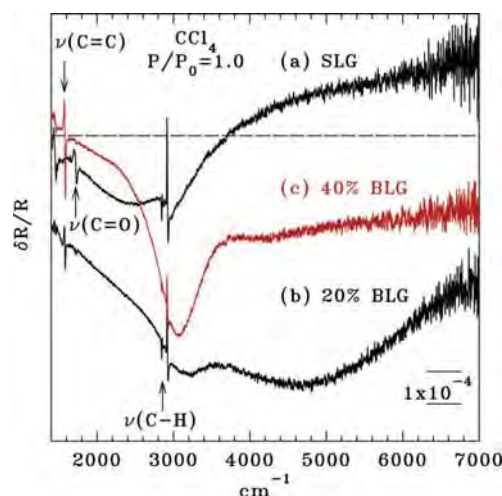


**Figure 8.** Data for graphene layers of varying thickness. (a) SLG, typical of the samples used in the present work, with  $<5\%$  of the area covered with bilayer regions; (b) an SLG layer with a  $\sim 20\%$  of the area covered with bilayer regions; and (c) an SLG layer with  $\sim 40\%$  bilayer regions. All data were obtained in p-polarization in  $CCl_4$  vapor at  $P/P_0 = 1.0$ . The dashed line shows  $\delta R/R = 0$ . The spectra are shown as recorded, with no displacement. Spectrum (a) is the same as that shown in Figure 2. The weak, unlabeled feature at the extreme low-energy end of (a) and (b) is a miscanceled Si multiphonon absorption.

The above discussion suggests a reason for why the  $\nu(C-H)$  structure (Figures 2 and 4) is relatively weak for  $H_2O$ , even though an electronic absorption is clearly evident. If regions with  $sp^3$ -hybridized  $C-H$  bonds are highly hydrophobic, they would not be wetted to the same extent as the rest of the SLG, even at  $P/P_0 = 1.0$ , and would remain essentially unaffected by the  $H_2O$ . Pristine regions are weakly hydrophilic, as shown by the dispersion-corrected DFT results described above, and would be wetted at elevated  $P/P_0$ .

Figure 8 shows the effects of increasing the graphene thickness, which permits an assessment of the importance of the small BLG regions found in the present SLG samples (Supporting Information, section 3) and also facilitates comparison with previous results. The fine structure, which is not clear in Figure 8, is shown in detail in the Supporting Information, section 14. Several points are noteworthy. First, the  $C=C$  stretching mode at about  $1580\text{ cm}^{-1}$  is IR-forbidden<sup>21</sup> in SLG and not detectable in the present SLG data. However, it is IR-allowed in BLG and FLG and is clearly observed here for samples with increased bilayer coverage. This feature shows a clear antiresonant line shape, as in previous work,<sup>24–27</sup> although the sign of the asymmetry differs from that in some studies.<sup>24,27</sup> The  $\nu(C=O)$  mode also shows a clear antiresonance. In both cases, the dynamic dipole lies in the graphene plane, which permits coupling to electronic excitations as discussed above. Second, the  $C-H$  stretching modes become weaker with increasing thickness. This is consistent with previous results<sup>24</sup> in which no graphene  $C-H$  modes were seen for 3–4-layer films. Because the line shapes do not change significantly, one concludes that the degree of coupling to the electronic continuum is essentially constant and that, therefore, the loss of intensity is due to a real decrease in the number of  $C-H$  bonds per unit area.

Third, the overall shapes of the broad-band absorptions for samples with significant BLG coverage are distinctly different from that seen for SLG. For  $\sim 40\%$  BLG, an intense and

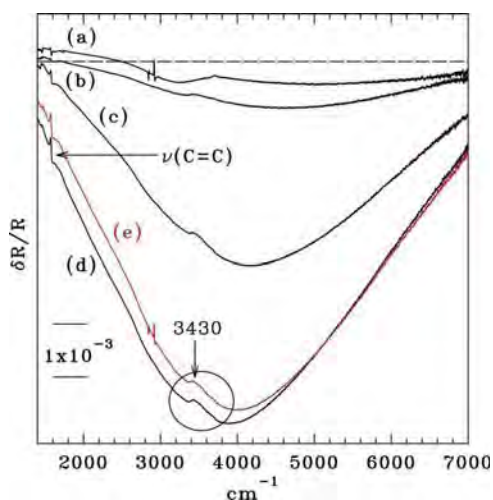


**Figure 9.** Data showing the effect of a strong, but noncondensable, dopant ( $\text{NH}_3$ ) on a  $\sim 20\%$  bilayer sample. Trace (a) shows, for reference, data for  $\text{CCl}_4$  at  $P/P_0 = 1.0$  as in previous figures. Traces (b)–(d) show data recorded, after completely purging the  $\text{CCl}_4$  with pure  $\text{N}_2$ , in a 100 mL/min flow of 0.1%  $\text{NH}_3$  in  $\text{N}_2$ . The approximate total exposure times are (b) 4, (c) 60, and (d) 220 min. Trace (e) shows the effect of purging the  $\text{NH}_3:\text{N}_2$ , following (d), with  $\text{CCl}_4:\text{N}_2$  at  $P/P_0 = 1.0$ . The spectra were recorded in p-polarization and have not been displaced vertically. The dashed line shows  $\Delta R/R = 0$ , and the encircled, upward-pointing band is due to the displacement of  $\text{H}_2\text{O}$  by  $\text{NH}_3$  (see text).

well-defined band is seen at  $\sim 3030 \text{ cm}^{-1}$  (0.38 eV) with a FWHM of  $\sim 0.07 \text{ eV}$ , which corresponds closely to the prominent mid-IR absorption band found<sup>23</sup> in transmission spectra of well-formed BLG. Simulation (Supporting Information, section 5) shows that the appearance of this feature in  $\Delta R/R$  is an optical effect resulting from the influence of the  $\text{CCl}_4$  layer on the MIRS “effective thickness” of the graphene layer. This feature is weak in the  $\sim 20\%$  bilayer sample, for which the second layer is more fragmented and incomplete, and is absent in SLG. Thus, it is concluded that the small coverage of BLG patches found in the SLG samples has no significant effect on the present results.

Finally, the data in Figure 9 show that doping is not, in itself, a major contributor to the effects observed here. For another  $\sim 20\%$  BLG sample,  $\text{NH}_3$  (an n-type dopant<sup>24</sup>) leads to a very intense absorption band with a maximum at  $\sim 0.48\text{--}0.58 \text{ eV}$ . After a total exposure of  $\sim 220 \text{ min}$  to 0.1%  $\text{NH}_3$  in  $\text{N}_2$ , the growth of this band had slowed but not yet stopped. The  $\sim 20\%$  BLG film used here is similar to that employed in Figure 8, and the  $\text{CCl}_4$  spectrum (Figure 9a) is also similar to that in Figure 8a. The antiresonant  $\nu(\text{C}=\text{C})$  mode gains intensity with increasing  $\text{NH}_3$  coverage,<sup>24</sup> and a broad, inverted band is seen at  $\sim 3430 \text{ cm}^{-1}$ , which is ascribed to displacement of  $\text{H}_2\text{O}$  from the graphene/ $\text{SiO}_2$  interface by  $\text{NH}_3$  (Supporting Information, section 13). The  $\text{NH}_3$  itself is not detected, presumably due to a low coverage under these conditions.<sup>52</sup> The broad-band feature seen for  $\text{NH}_3$  is different from that observed for  $\text{CCl}_4$  and leads to no detectable C–H features. Purging the  $\text{NH}_3:\text{N}_2$  with  $\text{CCl}_4:\text{N}_2$  at  $P/P_0 = 1.0$  leads to the immediate appearance of the C–H features but with only a small reduction in the broad-band intensity. Further purging with saturated  $\text{CCl}_4:\text{N}_2$  for a total of 45 min (not shown) caused only a small additional decrease in the broad-band intensity.

$\text{NH}_3$  bonds only very weakly<sup>52</sup> to HOPG and does not form a liquid-like layer at room temperature under the present conditions. The continued growth of the broad-band absorption over a period of several hours in a constant background of 0.1%  $\text{NH}_3:\text{N}_2$ , the slow reversal of the  $\text{NH}_3$  effect during purging (vs the behavior of acetone, Figure 7), and the displacement of interfacial  $\text{H}_2\text{O}$  all indicate that  $\text{NH}_3$  diffuses into the space between graphene and  $\text{SiO}_2$ . This has already been shown<sup>53</sup> on the basis of the  $\text{NH}_3$  response of a graphene/ $\text{SiO}_2$  field-effect transistor. Interfacial  $\text{NH}_3$  is able to bond strongly<sup>54</sup> to Si–OH via an O–H hydrogen bond, leaving the nonbonding N lone-pair orbital free to donate charge to the graphene. It does not, however, form a “wetting” layer on the exposed graphene surface, as do the other small molecules studied here, and does not affect the graphene electronic structure in the same manner as do these other adsorbates.

#### 4. CONCLUSIONS

The interaction of small molecules ( $\text{CCl}_4$ ,  $\text{CS}_2$ ,  $\text{H}_2\text{O}$ , and acetone) with SLG has been observed under steady-state conditions using IR MIRS. The major results, most of which have not previously been reported, are as follows.

- (1) A broad and intense absorption band, spanning the range of roughly 200–500 meV, is seen as a result of exposure and is ascribed to an electronic excitation resulting from a modification of the SLG band structure near  $E_F$ . The qualitative appearance of this feature and its dependence on IR polarization vary somewhat from sample to sample, which suggests an extrinsic effect such as adsorption-induced strain. However, it is seen for all samples studied here and increases in intensity as  $\text{CCl}_4 < \text{H}_2\text{O} < \text{acetone}$ .
- (2) In an effort to identify the source of the electronic absorption band, ab initio DFT calculations have been performed to model the interaction of  $\text{H}_2\text{O}$  with SLG with and without an  $\text{SiO}_2$  substrate. In agreement with previous work, proper treatment of dispersion (i.e., van der Waals interaction) is found to be important in obtaining the adsorption energy. An adhesion energy of  $\sim 1.5 \text{ eV/nm}^2$  is found for the SLG/ $\text{SiO}_2$  interface, and the configuration of the adsorbed  $\text{H}_2\text{O}$  is found to be vertical for free-standing SLG but nearly flat for SLG/ $\text{SiO}_2$ . It is found, however, that the electronic absorption effects seen here cannot be understood in terms of an ideal  $\text{H}_2\text{O}/\text{SLG}/\text{SiO}_2$  structure.
- (3) Nonadiabatic coupling is observed between C–H stretching vibrations and the absorption-induced electronic excitation. This leads to a complex antiresonance line shape for the  $\nu_{\text{as}}(\text{CH}_2)$ , and to some extent the  $\nu_{\text{s}}(\text{CH}_2)$ , mode of  $\text{CH}_2$  groups present as defects in the SLG. On the other hand, vibrational modes of weakly adsorbed molecular species do not undergo this coupling and thus exhibit no line shape anomalies. Hence, the vibrating species must be an integral part of the SLG lattice for strong coupling to occur. A linkage exists between the strength of the coupling and the dependence of the mode intensity on IR polarization because both are related to the orientation of the dynamic dipole moment with respect to the SLG plane. Thus, the effect of annealing on the polarization and line shapes of the  $\nu(\text{C–H})$  modes provides indirect evidence of restructuring of the SLG.

These results, although not yet fully understood, are potentially useful in several respects. The effects of weakly adsorbed small molecules on the SLG electronic structure could provide a protocol for the chemical modification of SLG electronic properties, for understanding environmental effects on these properties, and for transduction in SLG chemical sensors. The vibrational modes of adsorbed H<sub>2</sub>, as seen in IR spectroscopy, have long been used to probe semiconductor surface structure, particularly under steady-state conditions during chemical processing. With the added dimension of nonadiabatic coupling to the adsorption-induced electronic excitation,  $\nu(\text{C-H})$  modes are potentially of value as sensitive indicators of changes in SLG physical and electronic structure during treatment.

## ■ ASSOCIATED CONTENT

**S Supporting Information.** XPS data for the SiO<sub>2</sub> substrate layer, XPS data for carbonaceous impurities, sample characterization via Raman spectroscopy and microscopy, formation of an ice-like H<sub>2</sub>O layer, simulated MIRS spectra, effect of PMMA residue, data for sample G2, polarized IR electric field, DFT computational methods, model antiresonance line shapes, the effect of graphene corrugation on polarization in MIRS data, electrostatic effects on vibrational frequencies, displacement of H<sub>2</sub>O at the SLG/SiO<sub>2</sub> interface, and details of the ~20% and ~40% bilayer spectra. This material is available free of charge via the Internet at <http://pubs.acs.org>.

## ■ AUTHOR INFORMATION

### Corresponding Author

\*Phone: (202) 767-6728. Fax: (202) 767-1165. E-mail: victor.bermudez@nrl.navy.mil.

## ■ ACKNOWLEDGMENT

This work was supported by the Office of Naval Research. We are grateful to J. C. Culberston for help with the Raman experiments, to F. K. Perkins for providing the graphene growth furnace and the NH<sub>3</sub>:N<sub>2</sub> mixture, and to A. Snow for providing the CS<sub>2</sub>.

## ■ REFERENCES

- (1) Snow, E. S.; Perkins, F. K.; Robinson, J. A. *Chem. Soc. Rev.* **2006**, 35, 790–798.
- (2) Schedin, F.; Geim, A. K.; Morozov, S. V.; Hill, E. W.; Blake, P.; Katsnelson, M. I.; Novoselov, K. S. *Nat. Mater.* **2007**, 6, 652–655.
- (3) Robinson, J. T.; Perkins, F. K.; Snow, E. S.; Wei, Z.; Sheehan, P. E. *Nano Lett.* **2008**, 8, 3137–3140.
- (4) Wehling, T. O.; Novoselov, K. S.; Morozov, S. V.; Vdovin, E. E.; Katsnelson, M. I.; Geim, A. K.; Lichtenstein, A. I. *Nano Lett.* **2008**, 8, 173–177.
- (5) Liu, H.; Liu, Y.; Zhu, D. *J. Mater. Chem.* **2011**, 21, 3335–3345.
- (6) Alldredge, E. S.; Bădescu, Ș. C.; Bajwa, N.; Perkins, F. K.; Snow, E. S.; Reinecke, T. L.; Passmore, J. L.; Chang, Y. L. *Phys. Rev. B* **2008**, 78, 161403-1(R)–161403-4(R).
- (7) Tobin, R. G. *Surf. Sci.* **2002**, 502–503, 374–387.
- (8) Derycke, V.; Martel, R.; Appenzeller, J.; Avouris, Ph. *Appl. Phys. Lett.* **2002**, 80, 2773–2775.
- (9) Ryu, S.; Liu, L.; Berciaud, S.; Yu, Y.-J.; Liu, H.; Kim, P.; Flynn, G. W.; Brus, L. E. *Nano Lett.* **2010**, 10, 4944–4951.
- (10) Harrick, N. J. *Internal Reflection Spectroscopy*; Wiley: New York, 1967.
- (11) Queeney, K. T.; Fukidome, H.; Chaban, E. E.; Chabal, Y. J. *J. Phys. Chem. B* **2001**, 105, 3903–3907.
- (12) National Institute of Standards and Technology (NIST) Standard Reference Database No. 69; NIST Chemistry WebBook; <http://webbook.nist.gov/chemistry/>.
- (13) Powell, C. J. *Appl. Surf. Sci.* **1995**, 89, 141–149.
- (14) Li, X.; Cai, W.; An, J.; Kim, S.; Nah, J.; Yang, D.; Piner, R.; Velamakanni, A.; Jung, I.; Tutuc, E.; Banerjee, S. K.; Colombo, L.; Ruoff, R. S. *Science* **2009**, 324, 1312–1314.
- (15) Doniach, S.; Šunjić, M. *J. Phys. C* **1970**, 3, 285–291.
- (16) Speranza, G.; Minati, L. *Surf. Sci.* **2006**, 600, 4438–4444.
- (17) Hsiao, M.-C.; Liao, S.-H.; Yen, M.-Y.; Liu, P.-I.; Pu, N.-W.; Wang, C.-A.; Ma, C.-C. M. *Appl. Mater. Interfaces* **2010**, 2, 3092–3099.
- (18) Kimmel, G. A.; Matthiesen, J.; Baer, M.; Mundy, C. J.; Petrik, N. G.; Smith, R. S.; Dohnálek, Z.; Kay, B. D. *J. Am. Chem. Soc.* **2009**, 131, 12838–12844.
- (19) Teschke, O. *Langmuir* **2010**, 26, 16986–16990.
- (20) Acik, M.; Lee, G.; Mattevi, C.; Chhowalla, M.; Cho, K.; Chabal, Y. J. *Nat. Mater.* **2010**, 9, 840–845.
- (21) Wang, H.; Wang, Y.; Cao, X.; Feng, M.; Lan, G. *J. Raman Spectrosc.* **2009**, 40, 1791–1796.
- (22) Yamamoto, K.; Ishida, H. *Vib. Spectrosc.* **1994**, 8, 1–36.
- (23) Mak, K. F.; Sfeir, M. Y.; Misewich, J. A.; Heinz, T. F. *Proc. Natl. Acad. Sci. U.S.A.* **2010**, 107, 14999–15004.
- (24) Liu, Z.; Lu, X.; Peng, P.; Wu, W.; Pei, S.-S.; Yu, Q.; Bao, J. *Phys. Rev. B* **2010**, 82, 155435-1–155435-4.
- (25) Geng, B.; Horng, J.; Zhang, Y.; Tang, T.-T.; Park, C.-H.; Girit, C.; Hao, Z.; Martin, M.; Zettl, A.; Crommie, M.; Louie, S.; Wang, F. *Phys. Status Solidi B* **2010**, 247, 2931–2934.
- (26) Tang, T.-T.; Zhang, Y.; Park, C.-H.; Geng, B.; Girit, C.; Hao, Z.; Martin, M. C.; Zettl, A.; Crommie, M. F.; Louie, S. G.; Shen, Y. R.; Wang, F. *Nat. Nanotechnol.* **2009**, 5, 32–36.
- (27) Kuzmenko, A. B.; Benfatto, L.; Cappelluti, E.; Crassee, I.; van der Marel, D.; Blake, P.; Novoselov, K. S.; Geim, A. K. *Phys. Rev. Lett.* **2009**, 103, 116804–1–116804–4.
- (28) Mak, K. F.; Lui, C. H.; Shan, J.; Heinz, T. F. *Phys. Rev. Lett.* **2009**, 102, 256405–1–256405–4.
- (29) Pellegrino, F. M. D.; Angilella, G. G. N.; Pucci, R. *Phys. Rev. B* **2010**, 81, 035411–1–035411–12.
- (30) Cocco, G.; Cadelano, E.; Colombo, L. *Phys. Rev. B* **2010**, 81, 241412-1(R)–241412-4(R).
- (31) Locatelli, A.; Knox, K. R.; Cvetko, D.; Menteş, T. O.; Niño, M. A.; Wang, S.; Yilmaz, M. B.; Kim, P.; Osgood, R. M., Jr.; Morgante, A. *ACS Nano* **2010**, 4, 4879–4889.
- (32) Khan, M. A.; Mukaddam, M. A.; Schwingenschlög, U. *Chem. Phys. Lett.* **2010**, 498, 157–161.
- (33) Wehling, T. O.; Lichtenstein, A. I.; Katsnelson, M. I. *Appl. Phys. Lett.* **2008**, 93, 202110-1–202110-3.
- (34) Wehling, T. O.; Katsnelson, M. I.; Lichtenstein, A. I. *Chem. Phys. Lett.* **2009**, 476, 125–134.
- (35) Leenaerts, O.; Partoens, B.; Peeters, F. M. *Phys. Rev. B* **2009**, 79, 235440–1–235440–5.
- (36) Rubeš, M.; Nachtigall, P.; Vondrášek, J.; Bludský, O. *J. Phys. Chem. C* **2009**, 113, 8412–8419.
- (37) Jenness, G. R.; Karalti, O.; Jordan, K. D. *Phys. Chem. Chem. Phys.* **2010**, 12, 6375–6381.
- (38) Riley, K. E.; Pitoňák, M.; Jurečka, P.; Hobza, P. *Chem. Rev.* **2010**, 110, 5023–5063.
- (39) Ambrosetti, A.; Silvestrelli, P. L. *J. Phys. Chem. C* **2011**, 115, 3695–3702.
- (40) Henry, D. J.; Lukey, C. A.; Evans, E.; Yarovsky, I. *Mol. Simul.* **2005**, 31, 449–455.
- (41) Kondratyuk, P.; Yates, J. T., Jr. *Chem. Phys. Lett.* **2005**, 410, 324–329.
- (42) Porter, M. D.; Bright, T. B.; Allara, D. L.; Chidsey, C. E. D. *J. Am. Chem. Soc.* **1987**, 109, 3559–3568.
- (43) Langreth, D. C. *Phys. Rev. Lett.* **1985**, 54, 126–129.
- (44) Črljen, Ž.; Langreth, D. C. *Phys. Rev. B* **1987**, 35, 4224–4231.



- (45) Chabal, Y. J. *Surf. Sci. Rep.* **1988**, *8*, 211–357.
- (46) Reutt, J. E.; Chabal, Y. J.; Christman, S. B. *Phys. Rev. B* **1988**, *38*, 3112–3132.
- (47) Hirschmugl, C. J.; Williams, G. P.; Hoffmann, F. M.; Chabal, Y. J. *Phys. Rev. Lett.* **1990**, *65*, 480–483.
- (48) Kim, H.; Balgar, T.; Hasselbrink, E. *Chem. Phys. Lett.* **2011**, *508*, 1–5.
- (49) Zhao, X.; Outlaw, R. A.; Wang, J. J.; Zhu, M. Y.; Smith, G. D.; Holloway, B. C. *J. Chem. Phys.* **2006**, *124*, 194704–1–194704–6.
- (50) Crocellà, V.; Cerrato, G.; Magnacca, G.; Morterra, C. *J. Phys. Chem. C* **2009**, *113*, 16517–16529.
- (51) Gray, A.; Balooch, M.; Allegret, S.; De Gendt, S.; Wang, W.-E. *J. Appl. Phys.* **2008**, *104*, 053109-1–053109-8.
- (52) Bolina, A. S.; Brown, W. A. *Surf. Sci.* **2005**, *598*, 45–56.
- (53) Romero, H. E.; Joshi, P.; Gupta, A. K.; Gutierrez, H. R.; Cole, M. W.; Tadigadapa, S. A.; Eklund, P. C. *Nanotechnology* **2009**, *20*, 245501–1–245501–8.
- (54) Minibaev, R. F.; Zhuravlev, N. A.; Bagatur'yantz, A. A.; Alfimov, M. V. *Russ. Phys. J.* **2009**, *52*, 1164–1169.